

Multi-wavelength Emission of Gamma-ray Burst Prompt Phase. II. Spectral Polarimetry

JIA-SHENG LI¹ AND MI-XIANG LAN¹

¹*Center for Theoretical Physics and College of Physics, Jilin University, Changchun, 130012, China; lanmixiang@jlu.edu.cn*

ABSTRACT

Polarization spectra had been predicted within the photosphere model. For the purpose of seeking more clues to distinguish between the models, both the time-resolved and time-integrated polarization spectra from optical band to MeV gamma-rays of the magnetic reconnection model are studied here. There are two newly found differences between the two models. First, the time-integrated polarization degree (PD) of the magnetic reconnection model would in general increase with frequency for on-axis observations, while it is not monotonous for the photosphere model. Second, the variations of both the time-integrated and the time-resolved polarization angles (PAs) with frequency of the magnetic reconnection model is not random, while the time-integrated PA varies randomly with frequency for the photosphere model. Therefore, future energy-resolved polarization analysis could distinguish between the two models. In addition, the PA rotation spectra are studied for the first time. The rotation value of PA within the burst duration will decrease with the increase of the observational energy band. Most significant PA rotation would happen for slightly off-axis observations in each energy band. The PA would rotate even for on-axis observations in optical band. Compared with the aligned magnetic field case, the PA rotation is quite rare in the gamma-ray band for the case with a toroidal field in the radiation region.

Keywords: Gamma-ray bursts (629); Magnetic fields (994); Starlight polarization (1571)

1. INTRODUCTION

Gamma-ray bursts (GRBs) are the high-energy radiation produced by the collapse of a massive star (Woosley 1993; Bloom et al. 1999; MacFadyen et al. 2001; Mazzali et al. 2003; Hjorth et al. 2003) or the merger of the two compact stars (Narayan et al. 1992; Abbott et al. 2017; Goldstein et al. 2017; Lazzati et al. 2018). At present, there are three main models for the GRBs prompt phase: the internal shock model (Narayan et al. 1992; Paczynski & Xu 1994; Rees & Meszaros 1994; Daigne et al. 2009), the photospheric model (Thompson 1994; Eichler & Levinson 2000; Mészáros & Rees 2000; Rees & Mészáros 2005; Lazzati et al. 2009; Beloborodov 2011; Pe’er & Ryde 2011; Mizuta et al. 2011; Nagakura et al. 2011; Xu et al. 2012; Ruffini et al. 2013; Bégué et al. 2013; Lundman et al. 2013; Lazzati et al. 2013), and the magnetic reconnection model (Giannios 2008; Zhang & Yan 2011; Beniamini & Granot 2016; Granot 2016).

Since both the light curves and energy spectra in GRB prompt phase could be interpreted by these three models, these observable quantities could not be used to distinguish the models. The polarization provides two additional observable quantities, the polarization degree (PD) and the polarization angle (PA), which are sensitive to radiation mechanisms (Toma et al. 2009; Lundman et al. 2018; Lan & Dai 2020; Parsotan et al. 2020; Gill et al. 2020; Lan et al. 2021; Gill et al. 2021; Parsotan & Lazzati 2022; Guan & Lan 2023; Sui & Lan 2024; Cheng et al. 2024). It is predicted that the PD value in the gamma-ray band is roughly zero for the photosphere model (Lundman et al. 2018; Parsotan et al. 2020; Parsotan & Lazzati 2022). However, an upper limit of $\sim (40 - 50)\%$ in the magnetic reconnection model is predicted (Sui & Lan 2024; Li et al. 2024). In addition, PA evolves randomly in both the optical and gamma-ray bands for the photosphere model (Parsotan & Lazzati 2022), while it is not random in the gamma-ray band for the synchrotron model (Lan & Dai 2020; Lan et al. 2021; Wang & Lan 2023a,b; Li et al. 2024). Therefore, up till now we have two method to distinguish between the models in GRB prompt phase: one is the PD value at gamma-ray band and the other is the PA evolution pattern.

In addition to the polarization curves, polarization spectra in GRB prompt phase were also studied (Lan & Dai 2020; Lan et al. 2021; Parsotan & Lazzati 2022). The time-resolved PD will increase with frequency from X-rays to MeV gamma-rays in the magnetic reconnection model (Lan & Dai 2020). In the photosphere model, the time-integrated PD will decrease with frequency in optical band, then there is a PD peak around 10^{-1} keV, in higher energy band (around $[10 - 10^2]$ keV) the time-integrated PD is zero and finally it will increase with frequency beyond ($10^2 - 10^3$) keV (Parsotan & Lazzati 2022). In order to provide more clues to distinguish between the two models, the time-integrated PD spectra should be studied for the magnetic reconnection model.

Under frame work of the magnetic reconnection model, the predicted time-resolved PA is a constant with frequency from X-rays to 10 MeV gamma-rays for on-axis observation of the axisymmetric jet (Lan & Dai 2020). In high-energy gamma-ray band, the rotation of the PA with time is most likely to happen for slightly off-axis observations (Wang & Lan 2023a) and then three key parameters that have significant influence on the PA rotations were found (Wang & Lan 2023b). And the maximum rotation value of the time-resolved PA within the burst duration is 90° in gamma-ray band (Wang & Lan 2023b). For the photosphere model, the predicted time-integrated PA vary randomly with frequency at both optical band and gamma-ray band (Parsotan & Lazzati 2022). However, under frame work of the magnetic reconnection model, the laws for PA rotation in the lower energy band during GRB prompt phase is not yet known and whether or not the change of the time-resolved PA within the burst duration vary with frequency is also unknown. In addition, how the time-integrated PA vary with frequency from the optical band to gamma-rays has also not been investigated so far.

Recently, the polarization spectra were studied using the POLAR's data (De Angelis et al. 2023). Due to the low statistics and the low energy resolution, they did not found significant dependence of the PD and PA on the energy. In recent years, polarization detectors in various energy bands are now in comission or will be launched soon. In γ -ray band, both the High-energy Polarimetry Detector (HPD) (de Angelis & Polar-2 Collaboration 2022) on board POLAR-2 and the Compton Spectrometer and Imager (COSI) (Tomsick et al. 2019) are planned to launch in the near future. In the X-ray band, the Imaging X-ray Polarimetry Explorer (IXPE) (Negro et al. 2023) is now in comission and the Low-energy Polarimetry Detector (LPD) (de Angelis & Polar-2 Collaboration 2022) on board POLAR-2 is planned. The Very Large Telescope (VLT) and Liverpool Telescope (LT) are the polarization telescopes working in optical band. Therefore, there will be abundant multi-wavelength data in the near future. It is necessary to predict the multi-wavelength polarization (including the polarization curves ¹ and polarization spectra ²) to interpret these multi-wavelength polarization data and then to distinguish between the models.

In a previous paper, we studied the multi-wavelength polarization curves and the influence of the key parameters on the time-integrated polarizations (Li et al. 2024). Here, the polarization spectra, including the PD spectra, the PA spectra and the PA rotation spectra, are studied. The model is presented in Section 2. In Section 3, we show time-resolved and time-integrated polarization spectra in the GRB prompt phase, and the influence of key parameters on polarization spectra are also investigated. Finally, we present conclusions and discussion in Section 4.

2. THE MODELS

As in the previous studies (Uhm & Zhang 2015, 2016; Uhm et al. 2018), the radiation region is assumed to be a relativistic thin shell expanding radially from the central engine at redshift z . The electrons in the shell are accelerated via the magnetic reconnection process to emit synchrotron photons in the magnetic field. The shell is assumed to begin the radiation at radius r_{on} and stop at r_{off} . And the shell is also accelerated and the variation of its bulk Lorentz factor Γ is a power-law with the radius r from the central engine (Drenkhahn 2002).

$$\Gamma(r) = \Gamma_0(r/r_0)^s, \quad (1)$$

where we take $s = 0.35$ for an aligned field in the shell, but for a toroidal field the shell roughly maintains a constant bulk Lorentz factor and $s = 0$ (Drenkhahn 2002). The Γ_0 is the normalization value of the bulk Lorentz factor at the reference radius r_0 . The parameters marked with “ ’ ” in this paper are the comoving-frame quantities. And correspondingly, the magnetic field strength B' of the shell decays with the radius r and can be expressed as:

$$B'(r) = B'_0(r/r_0)^{-b}, \quad (2)$$

¹ Polarization curves refer to the variation of the energy-resolved or energy-integrated polarization with time, including the PD curve and PA curve.

² Polarization spectra refer to the variation of the time-resolved or time-integrated polarization with energy, including the PD spectrum and PA spectrum.

where the decay index b is taken 1 (Drenkhahn 2002). The B'_0 is the normalization value of the magnetic field strength at the reference radius r_0 .

We assume the shape of the photon spectrum $H_{en}(\nu')$ consists of three-segment power-laws, and the expression is as follows:

$$H_{en}(\nu') = \begin{cases} (\nu'/\nu'_1)^{\alpha_1+1}, & \nu' < \nu'_1, \\ (\nu'/\nu'_1)^{\alpha_2+1}, & \nu'_1 < \nu' < \nu'_2, \\ (\nu'_2/\nu'_1)^{\alpha_2+1}(\nu'/\nu'_2)^{\beta+1}, & \nu' > \nu'_2, \end{cases} \quad (3)$$

where ν' , ν'_1 and ν'_2 equal to $\nu(1+z)/\mathcal{D}$, $\min(\nu'_{cool}, \nu'_{min})$ and $\max(\nu'_{cool}, \nu'_{min})$, respectively. The ν is the observational frequency and $\mathcal{D} = 1/\Gamma(1 - \beta_v \cos \theta)$ is the Doppler factor, where β_v is the corresponding dimensionless velocity and θ is the angle between the line of sight and the local velocity direction.

The α_1 , α_2 and β are the low-energy, mid-energy and high-energy photon spectral indices, respectively. If the GRB is in a slow-cooling phase (i.e. $\nu'_{min} < \nu'_{cool}$), $\alpha_1 = -2/3$, $\alpha_2 = -1 - \frac{p-1}{2}$ and $\beta = -1 - \frac{p}{2}$. The p is the index of the true energy spectrum ($N(\gamma_e) \propto \gamma_e^{-p}$) of the injected electrons in the shell, and its value is taken as 2.6 here. If the GRB is in a fast-cooling phase (i.e. $\nu'_{cool} < \nu'_{min}$), $\alpha_1 = -2/3$ and $\beta = -1 - \frac{p}{2}$. The value of α_2 in the fast-cooling phase tends to $-3/2$ in a stronger decaying magnetic field and to -1 when the magnetic field is weaker (Uhm & Zhang 2014). Observationally, the value of α_2 is concentrated around -1 in the Band-function (Yu et al. 2016; Poolakkil et al. 2021), where the fitting is done above the energy band of the soft X-rays. However, it is around $-3/2$ when the analysis energy band is extended down to the optical band (Oganesyan et al. 2017, 2018, 2019; Ravasio et al. 2019; Toffano et al. 2021). So the two values of the mid-energy photon spectral index α_2 are considered in fast-cooling case.

The ν'_{cool} and ν'_{min} read:

$$\nu'_{cool} = \frac{q_e B' \gamma_{cool}^2 \sin \theta'_B}{2\pi m_e c}, \quad \nu'_{min} = \frac{q_e B' \gamma_{ch}^2 \sin \theta'_B}{2\pi m_e c}, \quad (4)$$

where m_e and q_e are the mass and charge of the electron, respectively. c is the speed of light. The θ'_B is the pitch angle of the electrons. $\gamma_{cool} = (6\pi m_e c \Gamma)/(\sigma_T B'^2 t)$ is the cooling Lorentz factor of electrons and t is the dynamical time in the burst-source frame or the lab-frame of the engine, where σ_T is the Thomson cross section. Actually, γ_{ch} corresponds to the minimal Lorentz factor of the truly power-law distributed electrons in the emission region.

Uhm et al. (2018) proposed five variation patterns for γ_{ch} with radius. However, among these five γ_{ch} patterns, there are mainly two polarization evolution patterns corresponding to the hard-to-soft and intensity-tracking spectral peak-energy evolution mode³, respectively. For the hard-to-soft mode (denoted as the i model), its γ_{ch} reads

$$\gamma_{ch}(r) = \gamma_{ch}^i (r/r_0)^g, \quad (5)$$

where γ_{ch}^i is the normalization value of γ_{ch} at radius r_0 . And we take $g = -0.2$ for i model (Uhm et al. 2018). For the intensity-tracking mode (denoted as the m model), its γ_{ch} reads

$$\gamma_{ch}(r) = \gamma_{ch}^m \times \begin{cases} (r/r_m)^g, & r \leq r_m, \\ (r/r_m)^{-g}, & r \geq r_m, \end{cases} \quad (6)$$

where r_m is normalization radius of the m model and γ_{ch}^m is the value of γ_{ch} at r_m . And we take $g = 1.0$ for m model (Uhm et al. 2018).

³ The spectral peak energy decays with time all the way for the hard-to-soft mode, while its value is positively correlated with flux for the intensity-tracking mode.

The equations for the time-resolved and energy-resolved flux density f_ν , the Stokes parameters Q_ν and U_ν are shown in Appendix A. For the time-integrated ones, the \bar{f}_ν , \bar{Q}_ν , and \bar{U}_ν are expressed as:

$$\begin{aligned}\bar{f}_\nu &= \frac{\int_{t_5}^{t_{95}} f_\nu dt_{obs}}{T_{90}} \\ \bar{Q}_\nu &= \frac{\int_{t_5}^{t_{95}} Q_\nu dt_{obs}}{T_{90}} \\ \bar{U}_\nu &= \frac{\int_{t_5}^{t_{95}} U_\nu dt_{obs}}{T_{90}},\end{aligned}\tag{7}$$

where t_5 and t_{95} are the times at which the accumulated flux density reaches 5% and 95% of the total flux density, respectively. And the duration of the burst (T_{90}) equals to $t_{95} - t_5$. It should be noted that the duration T_{90} of the same burst will vary with the observational energy band, i.e., the lower the observational energy band, the longer the duration (Li et al. 2024).

Then the time-integrated PD for the models with an aligned field in the radiation region can be expressed as follows.

$$\overline{PD} = \frac{\sqrt{\bar{Q}_\nu^2 + \bar{U}_\nu^2}}{\bar{f}_\nu}\tag{8}$$

And for the models with a toroidal field, because the Stokes parameter \bar{U}_ν is zero due to the axial symmetry, its time-integrated PD is

$$\overline{PD} = \frac{\bar{Q}_\nu}{\bar{f}_\nu}\tag{9}$$

The change of the time-resolved and energy-resolved PA (ΔPA) within T_{90} are defined as

$$\Delta PA = PA_{max} - PA_{min}\tag{10}$$

where PA_{max} and PA_{min} are the maximum and minimum time-resolved PA values within the T_{90} , respectively.

3. NUMERICAL RESULTS

With the model mentioned above, time-integrated spectral polarimetry are investigated and also the influences of the key parameters are studied. Total 7 models are considered here (Uhm et al. 2018). Unless specified, the parameters are taken as their typical or fiducial values: $\Gamma_0 = 250$, the jet opening angle $\theta_j = 0.1$ rad, viewing angle $\theta_V = \theta_j/2 = 0.05$ rad, $B'_0 = 30$ G, the starting radius of the emission $r_{on} = 10^{14}$ cm, the ending radius of the emission $r_{off} = 3 \times 10^{16}$ cm, $\gamma_{ch}^i = 5 \times 10^4$, $r_0 = 10^{15}$ cm, $\gamma_{ch}^m = 2 \times 10^5$ and $r_m = 2 \times 10^{15}$ cm (Ghirlanda et al. 2018; Lloyd-Ronning et al. 2019; Rouco Escorial et al. 2023; Uhm et al. 2018). For the aligned magnetic field, its orientation is assumed to be $\delta = \pi/6$ with respect to the projection of the jet axis on the plane of sky. The other parameters for these 7 models are listed in Table. 1.

3.1. PD and PA Spectra

For the 7 models considered, the effects of the magnetic field decaying index b , mid-energy photon spectral index α_2 , γ_{ch} patterns, and MFCs (Γ variation patterns) on the time-resolved and time-integrated polarization spectra are studied. The time-resolved polarization spectra are investigated at the peak time of the light curve at 300 keV for each model, and the results are shown in Figure. 1. Since the change of the spectral indices with frequency would lead to an abrupt increase of the local PD in an ordered magnetic field Π_p at ν_1 (i.e., $h\nu_1 = E_{break}$) and ν_2 (i.e., $h\nu_2 = E_{peak}$), it can be clearly seen that there are three plateaus in the time-resolved PD spectra smoothly connected at the two frequencies. Because the difference between the values of the two critical frequencies ν_1 and ν_2 are small for the $[2b_m]$ model, its second PD plateau is not obvious. The time-integrated polarization spectra are calculated within the T_{90} of each energy band. And the results are shown in Figure. 2. The time-integrated PD generally increases toward the

Table 1. Model Parameters.

Model	b	s (MFC)	γ_{ch} profile	α_2
$1b_i$	1.0	0 (toroidal)	Equation 5	-1.0
$1c_i$	1.25	0 (toroidal)	Equation 5	-1.0
$1d_i$	1.5	0 (toroidal)	Equation 5	-1.0
$1b_i2$	1.0	0 (toroidal)	Equation 5	-3/2
$1b_m$	1.0	0 (toroidal)	Equation 6	-1.0
$2b_i$	1.0	0.35 (aligned)	Equation 5	-1.0
$2b_m$	1.0	0.35 (aligned)	Equation 6	-1.0

high energy band for all 7 models considered here. Both the time-resolved and time-integrated polarization angles (PAs) are constants with frequency for on-axis observation.

Since the contribution of the local flux density $f_\nu(r)$ at large radii to the total one will be larger for the model with a smaller b and the local PD of the emission from radius r to $r + dr$ ($PD(r)$) would approach its maximum value of Π_p at large radii, both the time-resolved and the time-integrated PDs of the $[1b_i]$ model are higher than those of the models $[1c_i]$ and $[1d_i]$. Because the mid-energy photon spectral indices of the $[1b_i]$ and $[1b_i2]$ models are different, leading to a different Π_p between the frequencies of ν_1 and ν_2 , the time-resolved PDs of the two models show obvious diverse between the two frequencies.

Depending on the evolution of the critical frequency (Sari et al. 1998), the peak times of the light curves at 300 keV for m model would be larger than that for the i model with the same dynamics. The corresponding radius of the maximum local flux density $f_\nu(r)$ would be larger for the m model. Since the break energy (E_{break}) is proportional to r^3 , the E_{break} would be larger for the m model at the peak times of the light curves at 300 keV. The second PD plateau of the $[1b_m]$ ($[2b_m]$) model begins at a larger frequency compared with that of the $[1b_i]$ ($[2b_i]$) model. Because the time-resolved and time-integrated polarization spectra are similar between the i model and the m model, we use $[1b_i]$ model and $[2b_i]$ model as example to investigate the influences of other key parameters.

Then the effects of the key parameters (i. e., q , Γ_0 , and θ_j) on the time-integrated polarization spectra are studied. The time-integrated polarization spectra of the two models with various q are shown in Figure 3. For on-axis observations with $q \equiv \theta_V/\theta_j \leq 1/(\Gamma_0\theta_j)$, the toroidal fields (i.e., corresponding to the $[1b_i]$ model) within the $1/\Gamma$ cone are almost closed circles, the local polarizations from each closed magnetic field circle cancel with each other, resulting in low PDs. Such symmetry is gradually broken with the increase of q , resulting in the increasing PD. However, for an aligned field (e.g., $[2b_i]$ model), the time-integrated PDs would concentrate around a constant for on-axis observations due to a roughly unchanged asymmetry offered by the field. The time-integrated PAs of the $[2b_i]$ model would rotate gradually with energy for slightly off-axis observations (e.g., $q = 1.1$ and 1.2), while they show abrupt 90° changes slightly beyond 10^{15} Hz (i.e., around the Ultraviolet band) for all calculated off-axis observations of the $[1b_i]$ model.

The variations of the time-integrated polarization spectra with Γ_0 are shown in Figure. 4. Because with the increase of Γ_0 , the $1/\Gamma$ cone will decrease and the proportion of the radiation within $1/\Gamma$ cone becomes smaller. PD of the emission from inside $1/\Gamma$ cone are higher than that from outside. Therefore, in general the time-integrated PDs will decrease with Γ_0 . The time-integrated PAs remain as a constant with frequency for various Γ_0 values. The variations of the time-integrated polarization spectra with θ_j are shown in Figure. 5. With our calculations, the polarization properties with $\Gamma_0\theta_j \sim 1$ would be significantly different from these with $\Gamma_0\theta_j \sim 10$, the polarization spectra with $\theta_j = 0.01$ rad (corresponding to $\Gamma_0\theta_j = 2.5$) show obvious diverse from that of other θ_j values (corresponding to $\Gamma_0\theta_j \geq 7.5$).

It should be noted that the influence of the parameters on the time-integrated PDs is very tiny in optical band and is most obvious in X-ray band. In optical band, the T_{95} of all 7 models is roughly 10 times of the corresponding end time of the high time-resolved PD phase and the accumulated flux from the end of the high time-resolved PD phase to the T_{95} is about one half of the total flux within T_{90} . Although the PD values at the high time-resolved PD phase

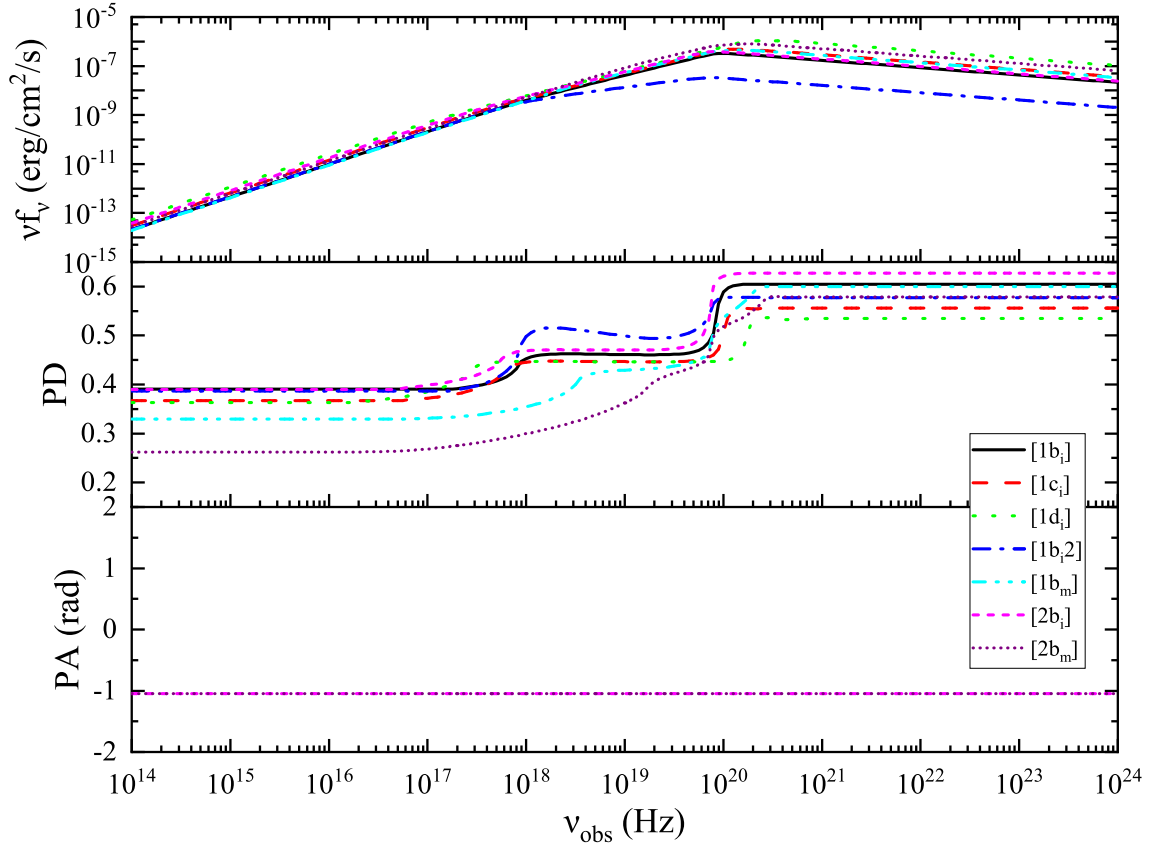


Figure 1. Spectra and polarization spectra of the 7 models at the peak time of the corresponding light curve of each model at 300 keV. Top, middle and bottom panels show the spectra, PD spectra and PA spectra, respectively. The black-solid, red-dashed, green-dotted, blue-dash-dotted, cyan-double-dot-dashed, magenta-short-dashed, and purple-short-dashed lines correspond to the models of $[1b_i]$, $[1c_i]$, $[1d_i]$, $[1b_2]$, $[1b_m]$, $[2b_i]$, and $[2b_m]$, respectively.

for different parameter sets would be different (Li et al. 2024), the long lasting low polarized phase after the high PD stage would wash out these difference, resulting in a roughly same time-integrated PD ($\sim 17\%$) for all 7 models in optical band.

3.2. ΔPA Spectra

The ΔPA spectra within T_{90} are investigated. The ΔPA spectra of the $[1b_i]$ model and of the $[2b_i]$ model for various q values are shown in Figure 6. In general, PA variation within T_{90} (ΔPA) is larger in a lower energy band for both model. For $[1b_i]$ model with a toroidal field in the radiation region, its PA could stay as a constant or change abruptly by 90° . In addition to the slightly off-axis observations, the ΔPA could be 90° even for on-axis observation and relatively large off-axis observation in optical band. In X-ray band, the ΔPAs are 90° only for slightly off-axis observations (i.e., $q = 1.1$ and 1.2). However, the ΔPAs are zero in gamma-ray band with the parameters used here for all the observational angles calculated. For $[2b_i]$ model with an aligned field in the radiation region, the ΔPA could be any value within 0° to 90° . The maximum ΔPA in each energy band would be reached at similar q values. In the optical band, the ΔPAs are nonzero for all the observational angles considered, including both on-axis and off-axis observations. The maximum value of ΔPA is 94.36° at $q = 1.3$. In both X-ray and gamma-ray band, the ΔPA is zero for on-axis observations (except for $q = 1$), while it will increase and then decrease with q for the off-axis observation. The maximum value of ΔPA is 82.79° at $q = 1.2$ in X-rays and is 64.19° also at $q = 1.2$ in gamma-rays.

Because in general the PA rotation for $q = 1.2$ is most significant in each energy band, we take $q = 1.2$ in the following to study the effects of the Γ_0 and θ_j on the ΔPA spectra. We first check whether or not ΔPA is only affected by the product $\Gamma_0 \theta_j$ and does not depend on the specific values of Γ_0 and θ_j . The ΔPA values for different sets of

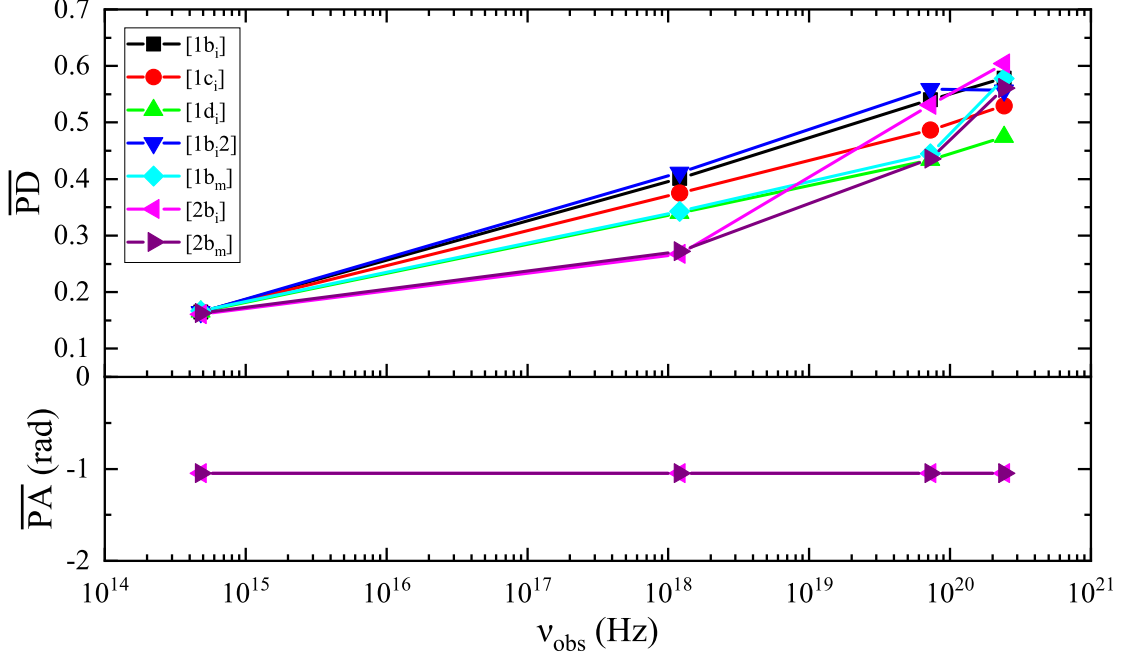


Figure 2. Time-integrated polarization spectra for the 7 models. Top and bottom panels show the time-integrated PD and PA spectra, respectively. The black, red, green, blue, cyan, magenta, and purple lines correspond to the models of $[1b_i]$, $[1c_i]$, $[1d_i]$, $[1b_i2]$, $[1b_m]$, $[2b_i]$, and $[2b_m]$, respectively.

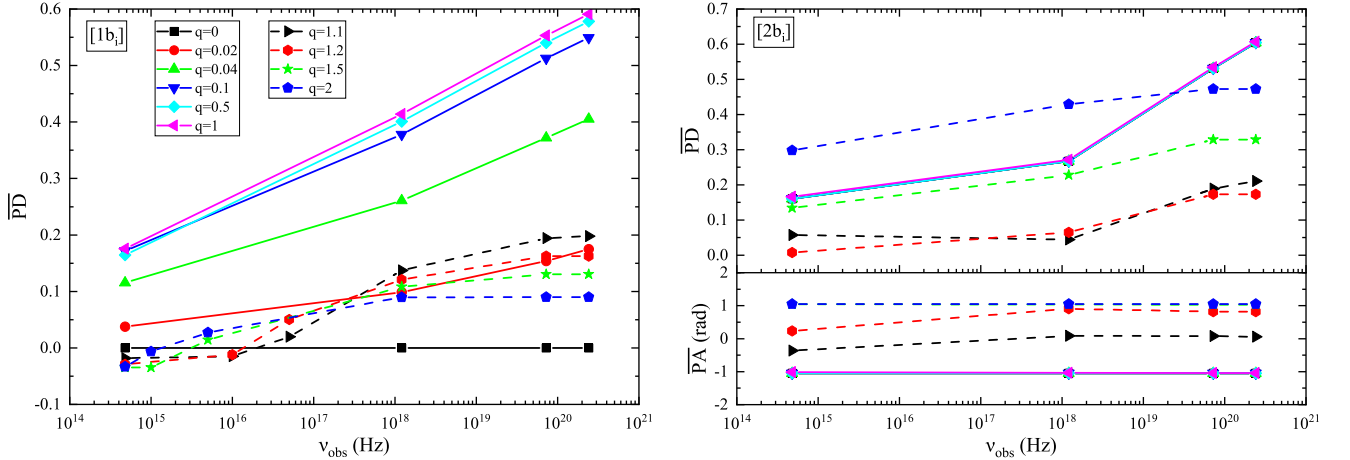


Figure 3. Time-integrated polarization spectra with various q values. Left and right panels correspond to the models of $[1b_i]$ and $[2b_i]$, respectively. PA shows abrupt 90° change when the PD changes its sign for the $[1b_i]$ model, so only the PD spectra are shown in the left panel. In the right panel, top and bottom panels show the time-integrated PD and PA spectra, respectively. The black, red, green, blue, cyan, and magenta solid lines correspond to the on-axis observations with $q = 0.00, 0.02, 0.04, 0.1, 0.5$ and 1 , respectively. The black, red, green, and blue dashed lines correspond to the off-axis observations with $q = 1.1, 1.2, 1.5$ and 2.0 , respectively.

(Γ_0, θ_j) are listed in Table 2 for $[1b_i]$ model and Table 3 for $[2b_i]$ model. For $[1b_i]$ model with a fixed product value of $\Gamma_0\theta_j$, the energy band with abrupt 90° PA rotation extends from single optical band to more energy bands with the increase of γ_0 . So for $[1b_i]$ model with a toroidal magnetic field in its radiation region, the Δ PA would depend on the concrete values of both Γ_0 and θ_j in the energy bands above X-rays, and for all the parameter sets considered here the Δ PA is 90° in optical band. For $[2b_i]$ model with an aligned field in the emission region, Δ PA values in the optical band depend on the specific values of Γ_0 and θ_j . However in the X-ray and gamma-ray bands, the difference

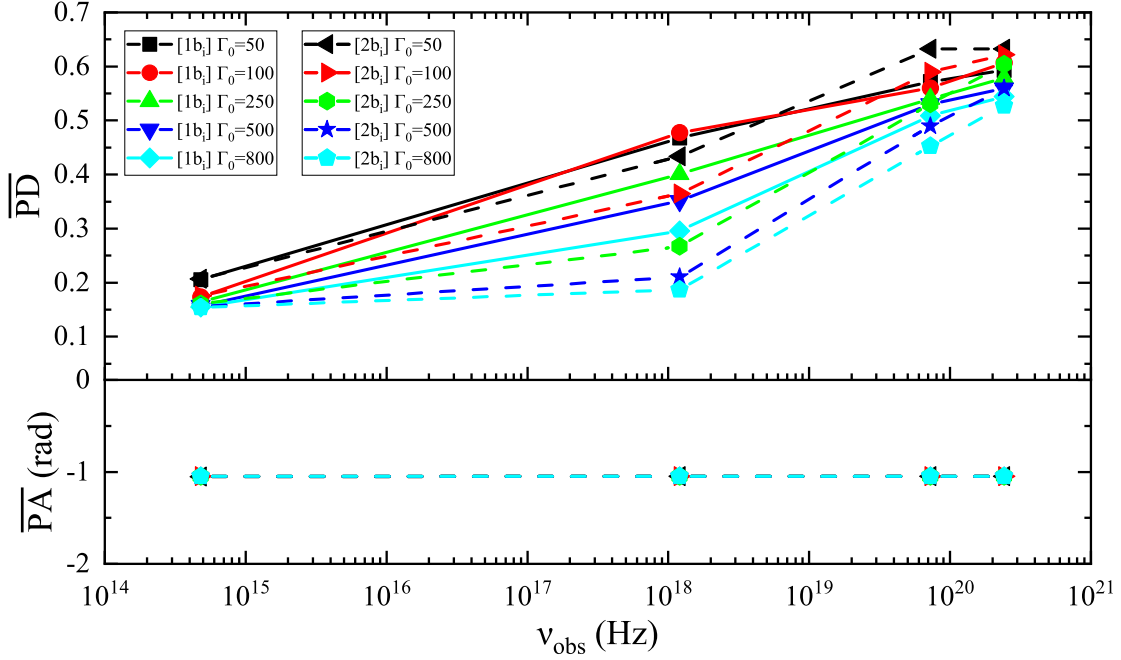


Figure 4. Time-integrated polarization spectra with various Γ_0 values. Top and bottom panels show the time-integrated PD and PA spectra, respectively. The solid and dashed lines correspond to models of $[1b_i]$ and $[2b_i]$, respectively. The black, red, green, blue, and cyan lines correspond to $\Gamma_0 = 50, 100, 250, 500,$ and 800 , respectively.

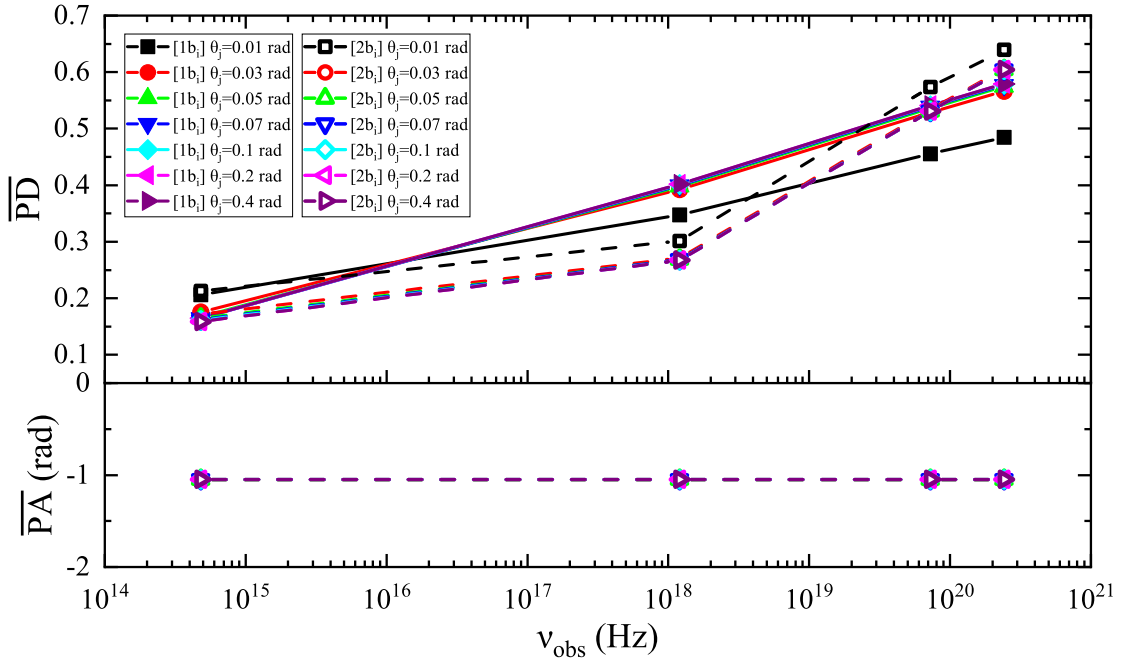


Figure 5. Time-integrated polarization spectra with various θ_j values. Top and bottom panels show the time-integrated PD and PA spectra, respectively. The solid and dashed lines correspond to models of $[1b_i]$ and $[2b_i]$, respectively. The black, red, green, blue, cyan, magenta, and purple lines correspond to $\theta_j = 0.01, 0.03, 0.05, 0.07, 0.1, 0.2,$ and 0.4 rad, respectively.

Table 2. The Δ PA spectra of the $[1b_i]$ model at $q = 1.2$ for different sets of (Γ_0, θ_j) with various fixed product values of $\Gamma_0\theta_j$.

$\Gamma_0\theta_j = 5$	R Band	5 keV	300 keV	1 MeV
$\Gamma_0 = 50$	90	0	0	0
$\Gamma_0 = 100$	90	0	0	0
$\Gamma_0 = 250$	90	90	0	0
$\Gamma_0\theta_j = 10$	R Band	5 keV	300 keV	1 MeV
$\Gamma_0 = 50$	90	0	0	0
$\Gamma_0 = 100$	90	0	0	0
$\Gamma_0 = 200$	90	90	0	0
$\Gamma_0 = 500$	90	90	0	0
$\Gamma_0\theta_j = 25$	R Band	5 keV	300 keV	1 MeV
$\Gamma_0 = 125$	90	0	0	0
$\Gamma_0 = 250$	90	90	0	0
$\Gamma_0 = 500$	90	90	0	0
$\Gamma_0 = 1000$	90	90	90	90
$\Gamma_0\theta_j = 50$	R Band	5 keV	300 keV	1 MeV
$\Gamma_0 = 125$	90	0	0	0
$\Gamma_0 = 250$	90	0	0	0
$\Gamma_0 = 500$	90	90	0	0
$\Gamma_0 = 1000$	90	90	90	90
$\Gamma_0\theta_j = 80$	R Band	5 keV	300 keV	1 MeV
$\Gamma_0 = 200$	90	0	0	0
$\Gamma_0 = 400$	90	0	0	0
$\Gamma_0 = 800$	90	90	90	90
$\Gamma_0 = 1000$	90	90	90	90

of Δ PA for the various sets of (Γ_0, θ_j) with a fixed product value of $\Gamma_0\theta_j$ is in general less than 10° . Therefore, the Δ PA values in the X-ray and gamma-ray bands are mainly dependent on the product value of $\Gamma_0\theta_j$ and independent on the concrete values of both Γ_0 and θ_j for $[2b_i]$ model.

With the above conclusions, the dependences of Δ PA spectra on both Γ_0 and θ_j are considered. The Δ PA spectra with varying Γ_0 values are shown in Figure 7. For the $[1b_i]$ model, with the increase of the Γ_0 , the energy band with abrupt 90° PA rotation extends from only optical band to all four energy band. For the $[2b_i]$ model, in general, Δ PA will be larger for a larger Γ_0 value in each energy band. The Δ PA would decrease with observational energy for most of the Γ_0 values considered, except $\Gamma_0 = 50$. It is worth noting that the Δ PAs for $\Gamma_0 = 500$ and 800 are close to 180° in the optical band, which is due to the existence of three $\sim 90^\circ$ rotations of PA within T_{90} . The corresponding PA curves for the two cases are shown in the inset figure of Figure 7.

The Δ PA spectra with varying θ_j values are shown in Figure 8. For the $[1b_i]$ model, the PAs in the gamma-ray band remain constant within T_{90} . Below the gamma-ray band, the lower the energy band, the larger the range of θ_j with Δ PA = 90° . For the $[2b_i]$ model, the Δ PA will increase with θ_j in general. For each θ_j value, the Δ PA will decrease with the increase of the observational energy band except for the narrow jets with $\theta_j = 0.01$ rad and 0.03 rad. As above in Figure 7, there are also three PA rotations within T_{90} for $\theta_j = 0.2$ rad and the Δ PA is roughly 180° .

4. CONCLUSIONS AND DISCUSSION

Table 3. The Δ PA spectra of the $[2b_i]$ model at $q = 1.2$ for different sets of (Γ_0, θ_j) with various fixed product values of $\Gamma_0\theta_j$.

$\Gamma_0\theta_j = 5$	R Band	5 keV	300 keV	1 MeV
$\Gamma_0 = 50$	20.29	18.29	27.86	27.86
$\Gamma_0 = 100$	46.29	19.1	26.15	28.04
$\Gamma_0 = 250$	61.31	21.5	25.85	29.06
$\Gamma_0\theta_j = 10$	R Band	5 keV	300 keV	1 MeV
$\Gamma_0 = 50$	35.45	41.91	14.19	14.19
$\Gamma_0 = 100$	63.82	46.47	14.02	14.02
$\Gamma_0 = 200$	82.23	45.63	17.36	14.02
$\Gamma_0 = 500$	84.33	55.3	25.04	14.09
$\Gamma_0\theta_j = 25$	R Band	5 keV	300 keV	1 MeV
$\Gamma_0 = 125$	169.33*	81.82	64.76	64.76
$\Gamma_0 = 250$	89.33	82.79	64.19	64.19
$\Gamma_0 = 500$	89.22	81.43	69.67	64.95
$\Gamma_0 = 1000$	89.21	83.18	73.14	66.01
$\Gamma_0\theta_j = 50$	R Band	5 keV	300 keV	1 MeV
$\Gamma_0 = 125$	168.75*	87.83	83.24	83.24
$\Gamma_0 = 250$	176.83*	87.77	79.15	79.15
$\Gamma_0 = 500$	178.33*	87.96	78.09	78.09
$\Gamma_0 = 1000$	89.87	87.04	80.02	80.02
$\Gamma_0\theta_j = 80$	R Band	5 keV	300 keV	1 MeV
$\Gamma_0 = 200$	89.07	90.31	89.36	89.36
$\Gamma_0 = 400$	178.39*	89.17	85.57	85.57
$\Gamma_0 = 800$	178.04*	89.06	84.39	84.39
$\Gamma_0 = 1000$	163.35*	88.79	85.2	85.2

NOTE—The superscript * indicates that there are three $\sim 90^\circ$ PA rotations within T_{90} .

The polarization spectra down to the optical band of the photosphere model had been investigated in Parsotan & Lazzati (2022). However, it is not considered in the magnetic reconnection model so far. In this paper, under frame work of the magnetic reconnection model both the time-resolved and the time-integrated polarization spectra (including the PD spectra, the PA spectra and the Δ PA spectra) are investigated. Total 7 models are considered and the influences of the key parameters on polarization spectra are studied.

In general, there are three PD plateaux in the time-resolved PD spectra, smoothly connected at the break energy and the peak energy. For on-axis observations, the time-integrated PD would in general increase with frequency and the result is independent of the key parameters, such as jet opening angle, the viewing angle and the bulk Lorentz factor. The time-integrated PDs would concentrate around 17% in optical R-band here and the influence of the parameters are very tiny. With respect to the different values of the parameters, the ranges of the time-integrated PDs would be (20%, 35%) in X-ray, (45%, 55%) in 300 keV, and (47%, 60%) in 1 MeV, respectively. However, the variation trend of the time-integrated PD with frequency is not monotonic in the photosphere model (Parsotan & Lazzati 2022). The first main difference found here between the two models would be the variation trend of the time-integrated PD with frequency, which provides a new method to distinguish between the two models.

For on-axis observations, the time-integrated PA would stay as a constant with frequency for the magnetic reconnection model, while it rotates randomly for the photosphere model (Parsotan & Lazzati 2022). For the magnetic

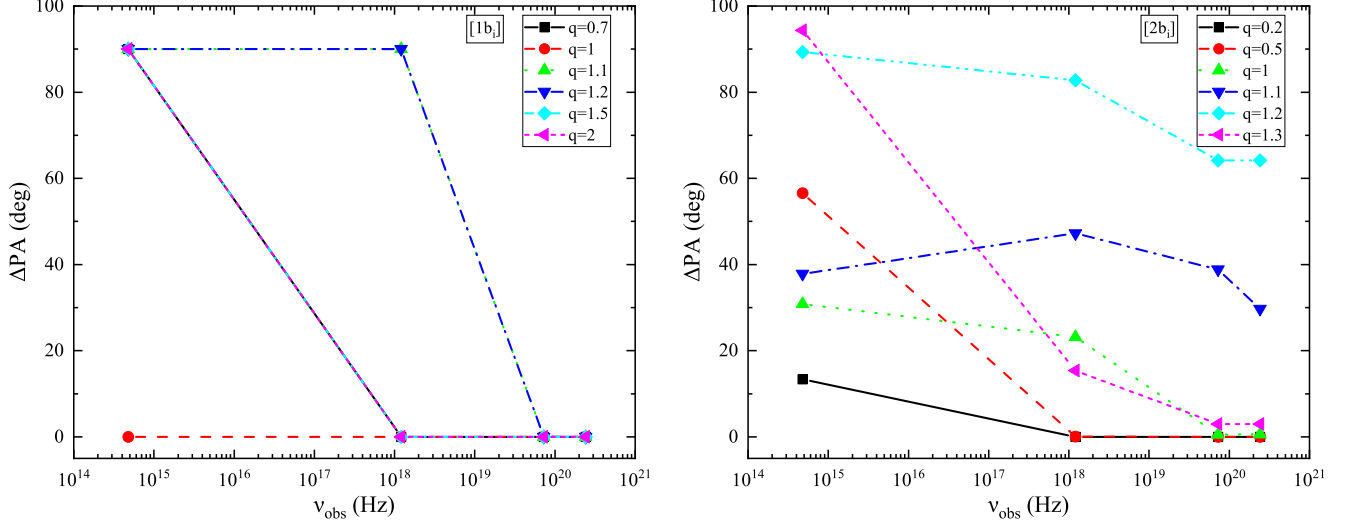


Figure 6. PA rotation spectra within T_{90} for various q values. Left and right panels correspond to the models of $[1b_i]$ and $[2b_i]$, respectively. In the left panel, the black, red, green, blue, cyan, and magenta lines correspond to $q = 0.7, 1, 1.1, 1.2, 1.5$ and 2 , respectively. In the right panel, the black, red, green, blue, cyan, and magenta lines correspond to $q = 0.2, 0.5, 1, 1.1, 1.2$ and 1.3 , respectively.

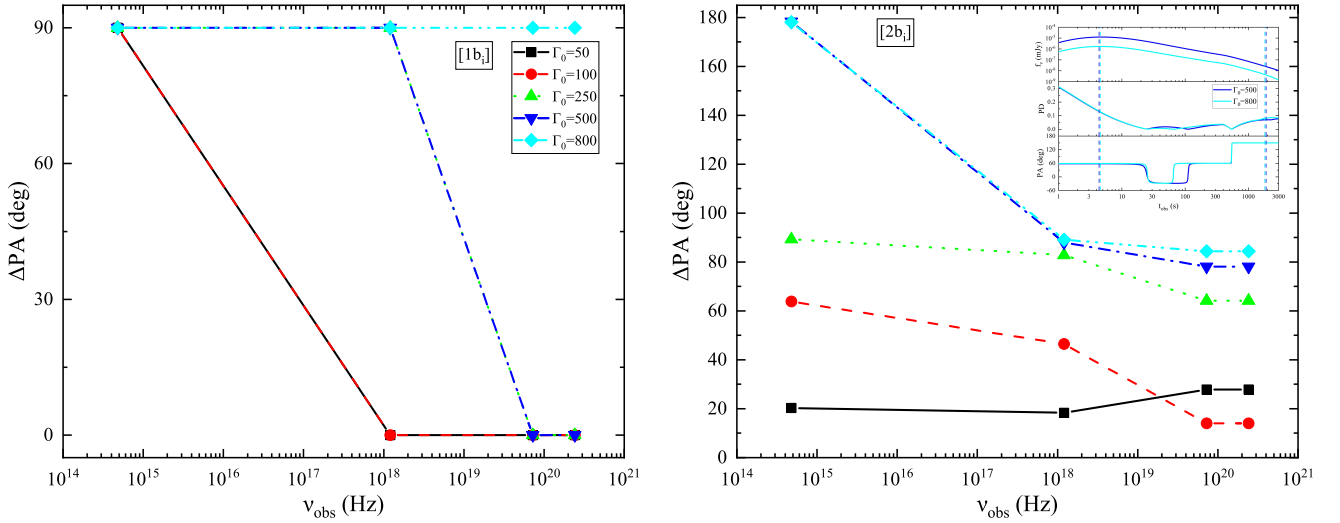


Figure 7. PA rotation spectra of $q = 1.2$ for various Γ_0 values. The left and right panels correspond to the models of $[1b_i]$ and $[2b_i]$, respectively. The black, red, green, blue, and cyan lines correspond to $\Gamma_0 = 50, 100, 250, 500$ and 800 , respectively. For the $[2b_i]$ model, the Δ PAs of the $\Gamma_0 = 500$ and 800 in the optical band are close to 180° , that is because there are three $\sim 90^\circ$ PA rotations within T_{90} . In the upper right corner of the right panel, the corresponding light curves and polarization curves with three PA rotations within T_{90} for $\Gamma_0 = 500$ and 800 are shown, and reference lines, with the same color as its light curves, indicate the T_{90} ranges in optical band.

reconnection model with off-axis observations, the time-integrated PD would decrease to zero and then increase with frequency for the toroidal field in the radiation region and the time-integrated PA would change abruptly by 90° when the time-integrated PD reaches zero. Such abrupt PA rotations would happen roughly in the UltraViolet energy band. For the aligned field case, independent of the observational geometry the time-integrated PDs would in general increase with frequency, and the time-integrated PA would rotate gradually with frequency only for slightly off-axis observations. Such gradual PA rotation would happen from optical band to X-rays. Therefore, in general the variation trend of the time-integrated PA with frequency is not random for the magnetic reconnection model, while it varies

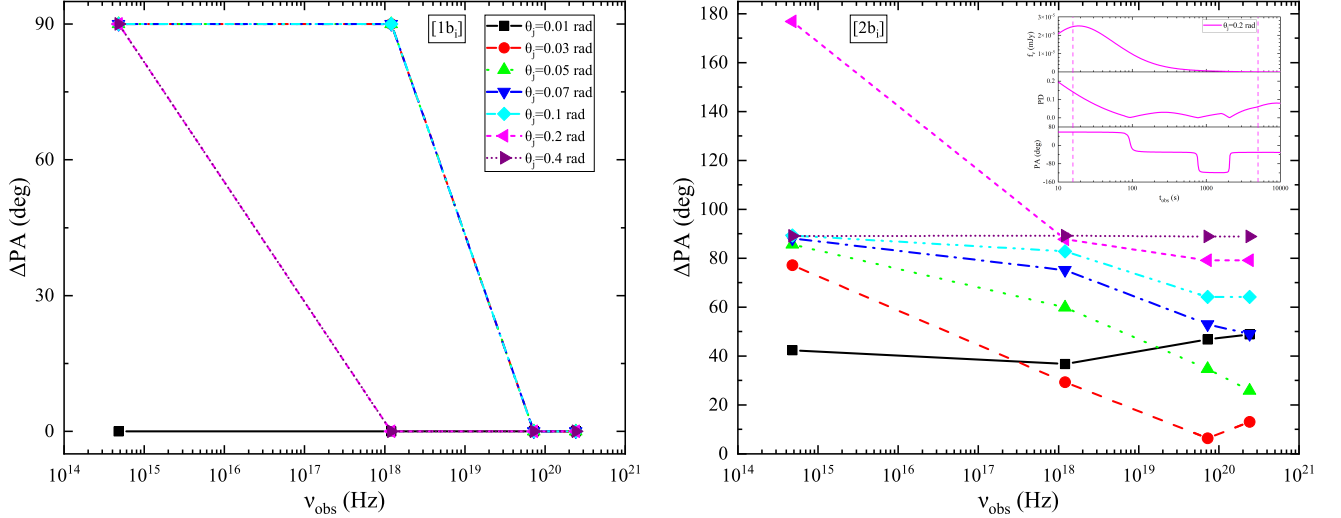


Figure 8. PA rotation spectra of $q = 1.2$ for various θ_j values. The left and right panels correspond to the models of [1b_i] and [2b_i], respectively. The black, red, green, blue, cyan, magenta, and purple lines correspond to $\theta_j = 0.01, 0.03, 0.05, 0.07, 0.1, 0.2,$ and 0.4 rad, respectively. For the [2b_i] model, the ΔPA of the $\theta_j = 0.2$ rad in the optical band is close to 180° , it is also because there are three 90° PA rotations within T_{90} . In the upper right corner of the right panel, light curves and polarization curves with three PA rotations within T_{90} for $\theta_j = 0.2$ rad are shown, and reference lines indicate the T_{90} range in optical band.

randomly for the photosphere model (Parsotan & Lazzati 2022). This is the second difference found here between the magnetic reconnection model and the photosphere model.

The PA rotation spectra are also studied. In general, the rotation value of PA within T_{90} will decrease with the increase of the observational energy band. Most significant PA rotation would happen for slightly off-axis observations in each energy band, which is consistent with our former study in gamma-ray band (Wang & Lan 2023a). For on-axis observations, PA rotations will only happen in optical band. For the models with a toroidal field in its radiation region, the change of the PA can only be abrupt 90° and most of the abrupt 90° PA rotations within the burst duration happen in the energy bands below X-rays. Such abrupt PA rotations are quite rare in gamma-ray band and there is only one parameter set under which there is one abrupt 90° PA rotation in gamma-ray band during the burst. For the models with an aligned field in the emission region, the rotation value of PA can range from 0° to 90° and there can be more than once 90° PA rotations within the burst duration. With the increase of the Γ_0 (or θ_j), the rotation value of the time-resolved PA will roughly increase. Even more, there are three $\sim 90^\circ$ PA rotations within the burst duration in optical band for some parameter sets. In both X-ray and gamma-ray bands, ΔPA values with an aligned field in the radiation region are determined by the product value of $\Gamma_0\theta_j$ and is independent of the concrete values of both Γ_0 and θ_j . However, for the model with a toroidal field in its emission region, the results depend on both values of the Γ_0 and θ_j , so does for the optical band in the model with an aligned field. In our study, the jet is assumed to be uniform and axisymmetric. It should be noted that the gradual PA rotation would happen only for the cases with an aligned field in the radiation region for off-axis observations in our model. However, PA of the on-axis observation could also change continuously for non-axisymmetric patchy jets (Gill & Granot 2024).

¹ We thank the anonymous referee for useful suggestions. This work is supported by the National Natural Science
² Foundation of China (grant Nos. 12473040, and 11903014). M.X.L also would like to appreciate the financial support
³ from Jilin University.

A. THE TIME-RESOLVED AND ENERGY-RESOLVED STOKES PARAMETERS

According to Lan & Dai (2020); Sui & Lan (2024), the flux density f_ν , the time-resolved and energy-resolved Stokes parameters Q_ν and U_ν will be expressed as:

$$\begin{aligned} f_\nu &= \frac{1+z}{4\pi D_L^2} \int \frac{\mathcal{D}^2}{\Gamma} \frac{c}{4\pi r} N P'_0 H_{en}(\nu') \sin \theta'_B d\phi dt \\ Q_\nu &= \frac{1+z}{4\pi D_L^2} \int \frac{\mathcal{D}^2}{\Gamma} \frac{c}{4\pi r} N P'_0 H_{en}(\nu') \sin \theta'_B \Pi_p \cos 2\chi_p d\phi dt \\ U_\nu &= \frac{1+z}{4\pi D_L^2} \int \frac{\mathcal{D}^2}{\Gamma} \frac{c}{4\pi r} N P'_0 H_{en}(\nu') \sin \theta'_B \Pi_p \sin 2\chi_p d\phi dt, \end{aligned} \quad (\text{A1})$$

where D_L is the luminosity distance of the source, $N = \int R_{inj} dt / \Gamma$ is the total electron number in the shell, and $P'_0 = 3\sqrt{3}m_e c^2 \sigma_T B' / (32q_e)$ represents the magnitude of the spectrum (Rybicki & Lightman 1979). The R_{inj} is the electron injection rate. And ϕ is the angle in the plane of sky between the projection of the jet axis and projection of the radial direction of a local fluid element. The Π_p is the local PD and reads:

$$\Pi_p = \tilde{\alpha} / (\tilde{\alpha} - 2/3), \quad (\text{A2})$$

where $\tilde{\alpha}$ is the photon spectral index. $\tilde{\alpha} = \alpha_1$ for $\nu' < \nu'_1$, $\tilde{\alpha} = \alpha_2$ for $\nu'_1 < \nu' < \nu'_2$, and $\tilde{\alpha} = \beta$ for $\nu' > \nu'_2$. The χ_p is the local PA and its expression can be found in Lan et al. (2016).

For an aligned field, the time-resolved and energy-resolved PD (PD) and PA (PA) read:

$$PD = \frac{\sqrt{Q_\nu^2 + U_\nu^2}}{f_\nu}, \quad (\text{A3})$$

and

$$PA_{pre} = \frac{1}{2} \arctan \left(\frac{U_\nu}{Q_\nu} \right). \quad (\text{A4})$$

The final PA (PA) needs to be adjusted according to the value of the Stokes parameter. When $Q_\nu > 0$, the final PA equals to PA_{pre} ; when $Q_\nu < 0$, if $U_\nu > 0$ then the PA is $PA = PA_{pre} + \pi/2$, if $U_\nu < 0$ then the PA is $PA = PA_{pre} - \pi/2$ (Lan et al. 2018).

For a toroidal field, U_ν is always 0 because of axial symmetry. So the time-resolved PD (Π) reads:

$$PD = \frac{Q_\nu}{f_\nu}. \quad (\text{A5})$$

PA will rotate $\pi/2$ when PD changes its sign.

Considering the equal arrival time surface (EATS) effect, the observer time t_{obs} is related to the burst-source time t as follows (Sari 1998; Uhm & Zhang 2016):

$$t_{obs} = \left[t - \frac{r}{c} \cos \theta - t_{on} + \frac{r_{on}}{c} \right] (1+z), \quad (\text{A6})$$

The shell begins to radiate photons at radius r_{on} at a burst-source time t_{on} .

B. SPECTRAL POLARIMETRY AT THE PEAK TIME OF THE LIGHT CURVE AT 300 KEV

The impact of the bulk Lorentz factor Γ_0 , jet opening angle θ_j , viewing angle θ_V , and MFCs on the spectra and polarization spectra at the peak time of the light curve in each model at 300 keV are investigated. The model parameters are shown in Table. 1. The orientation of the aligned magnetic field is set to be $\delta = \pi/6$. The other parameters are fixed as follows: $B_0 = 30$ G, $r_{on} = 10^{14}$ cm, $r_{off} = 3 \times 10^{16}$ cm, $\gamma_{ch}^i = 5 \times 10^4$, and $r_0 = 10^{15}$ cm (Uhm et al. 2018).

We take $\Gamma_0 = 250$ and $\theta_j = 0.1$ rad, then the numerical results with various q values are shown in Figures B1 and B2. Similar to the time-integrated polarization spectra, with the increase of q , time-resolved PDs of a toroidal field will increase when $q \leq 1/(\Gamma_0 \theta_j)$ and decrease when $q > 1$. The spectra and polarization spectra of an aligned field for on-axis observations are very similar. However, for the off-axis observations, time-resolved PDs will decrease and

then increase with q , while time-resolved PAs changes gradually with frequency for slightly off-axis observations (i.e., $q = 1.1, 1.2$).

For off-axis observations (i.e., $q = 1.1, 1.2, 1.5$, and 2.0), the flux density disappears suddenly and correspondingly the time-resolved PDs would rise with frequency steeply. This is because the observed frequency ν_{obs} exceeds the maximum frequency $\nu_{max} = (3\mathcal{D}q^2)/[(1+z)\sigma_T m_e c]$ of the synchrotron emission. Taking the $[1b_i]$ model with a toroidal magnetic field in its radiation region as an example, because the bulk Lorentz factor Γ is constant, the Doppler factor \mathcal{D} would increase with the radius r . Thus, on an EATS, ν_{max} at small radius is smaller, so the flux density vanishes at lower frequencies from small radius and the flux density would be from the large radius at higher frequencies. The shrinking radiation region with frequency would lead to the steep increase of the time-resolved PD with frequency at high energy band. The cease frequency of the flux (corresponding to the maximum frequency) for a larger q case is smaller. That is because the peak time of the light curve at 300 keV with a larger q value is larger, the values of θ on the corresponding EATS become relatively larger, leading to a smaller Doppler factor, hence leading to a smaller maximum frequency. The peak time of the light curve for a larger observational angle would be larger, leading to a smaller Doppler factor in the radiation region and to a smaller maximum frequency. So the flux density disappears at a smaller frequency for a larger observational angle.

We take $\theta_j = 0.1$ rad and $q = 0.5$, and the numerical results with various Γ_0 values are shown in Figure. B3. At the peak time of the light curve at 300 keV, the cooling is fast, so ν_{cool} corresponds to E_{break} . Due to $\nu_{cool} \propto \gamma_{cool}^2 \propto \Gamma^4$, E_{break} would move towards the higher energy band with the increase of Γ_0 , leading to a shorter second PD plateau with Γ_0 . Because the proportion of the radiation within $1/\Gamma$ cone of high local PD would decrease with Γ_0 , time-resolved PD will decrease with Γ_0 . Finally, we take $\Gamma_0 = 250$ rad and $q = 0.5$, and the numerical results for various θ_j values are shown in Figure. B4. The time-resolved PD values of the $[1b_i]$ model are similar for all calculated θ_j values except $\theta_j = 0.01$ rad. Since the syntropy of the toroidal magnetic field within the region of $1/\Gamma$ cone is lower when $q \leq 1/(\Gamma_0\theta_j)$, for $\theta_j = 0.01$ rad and $q = 0.5 \sim 1/(\Gamma_0\theta_j)$ of the $[1b_i]$ model its time-resolved PDs are relatively lower than other θ_j values.

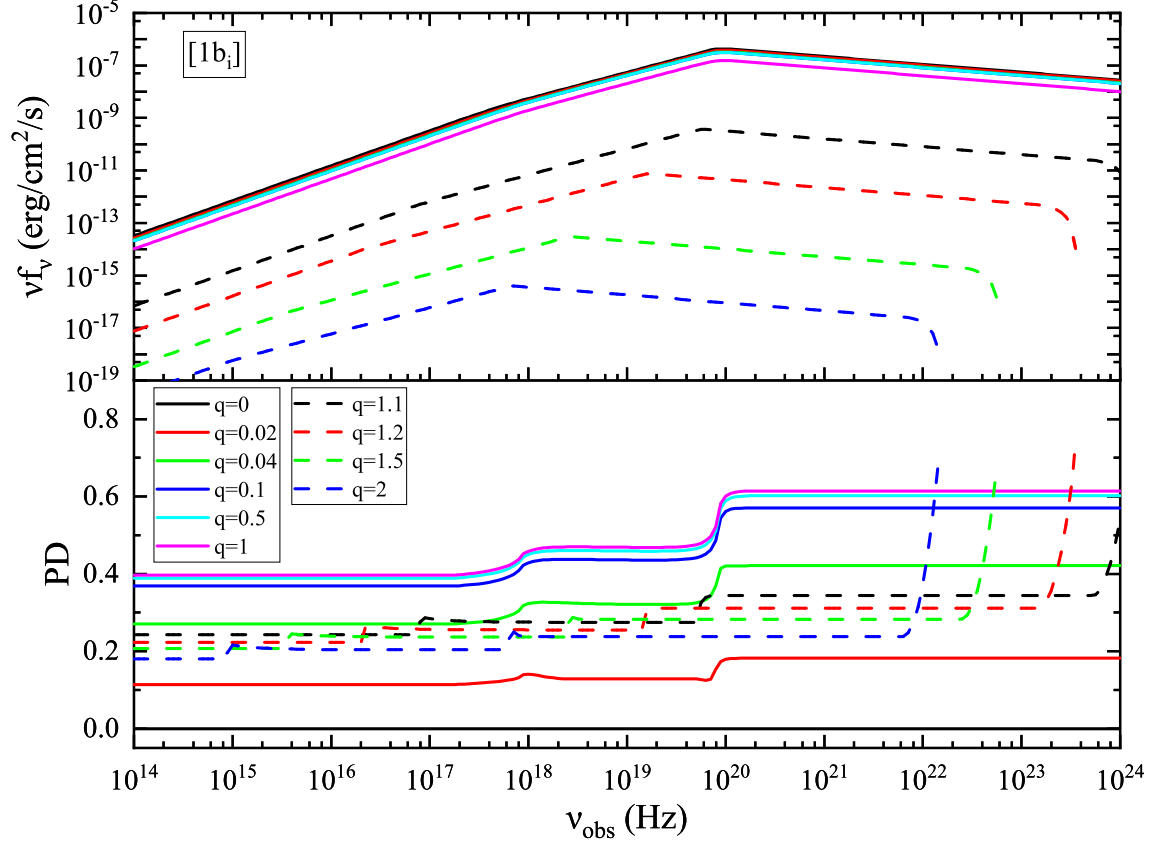


Figure B1. Spectra and polarization spectra of the $[1b_i]$ model at the peak time of the light curve at 300 keV for various q values. Top and bottom panels show the spectra and PD spectra, respectively. The black, red, green, blue, cyan, and magenta solid lines correspond to $q = 0, 0.02, 0.04, 0.1, 0.5$ and 1 , respectively. The black, red, green, and blue dashed lines correspond to $q = 1.1, 1.2, 1.5$ and 2.0 , respectively.

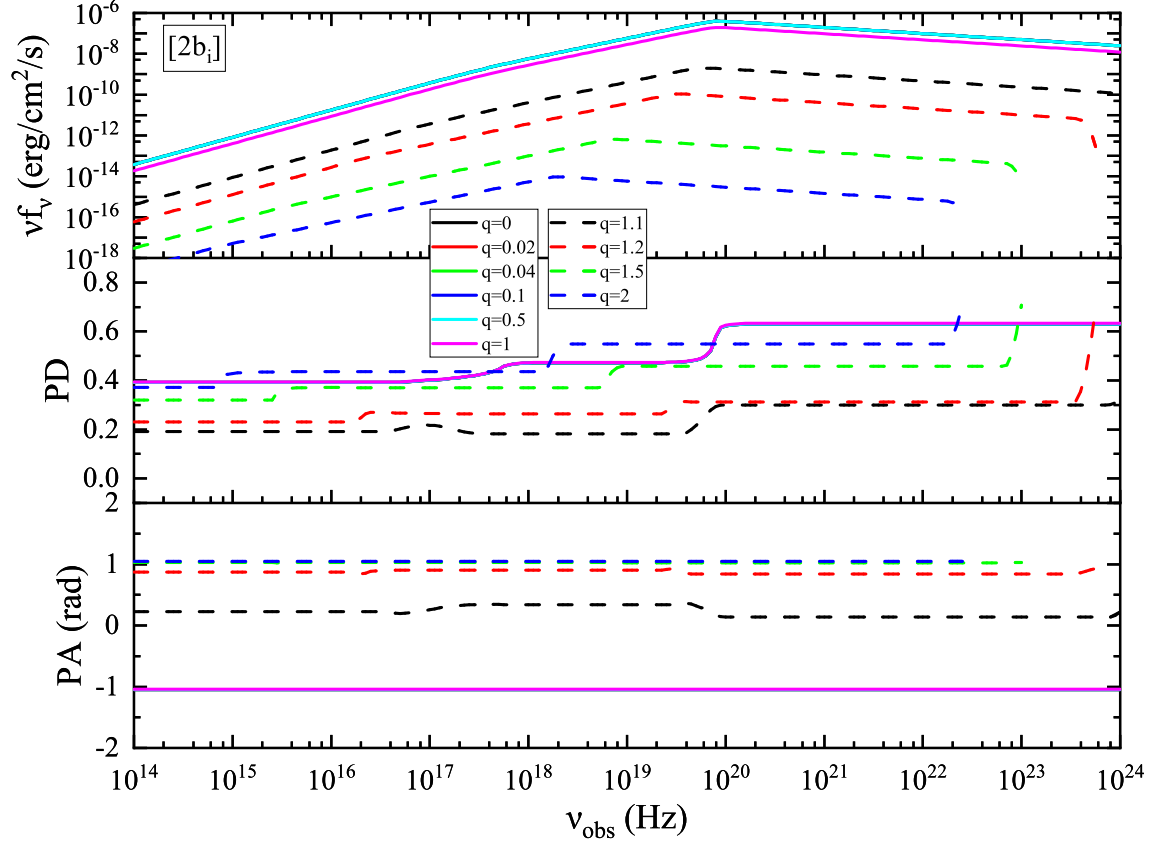


Figure B2. Spectra and polarization spectra of the $[2b_i]$ model at the peak time of the light curve at 300 keV for various q values. Top, middle and bottom panels show the spectra, PD spectra and PA spectra, respectively. The black, red, green, blue, cyan, and magenta solid lines correspond to $q = 0, 0.02, 0.04, 0.1, 0.5$ and 1 , respectively. The black, red, green, and blue dashed lines correspond to $q = 1.1, 1.2, 1.5$ and 2.0 , respectively.

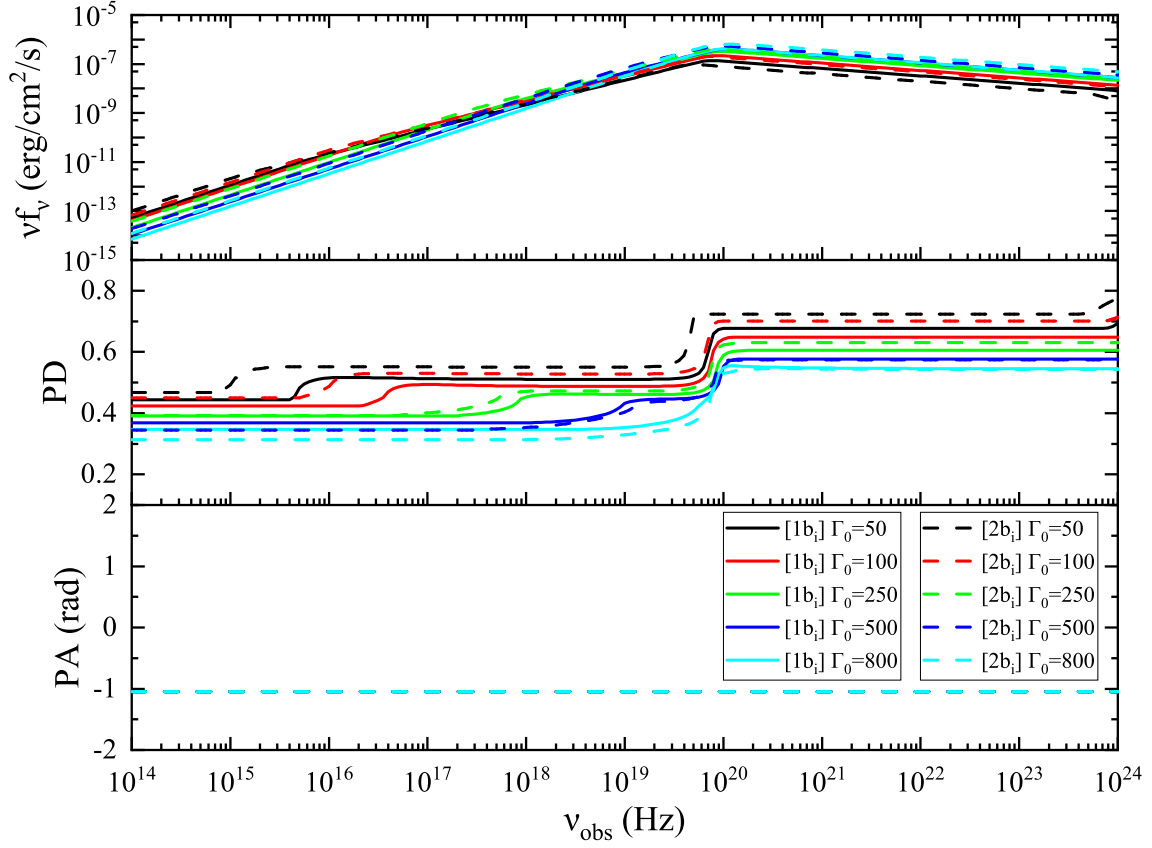


Figure B3. Spectra and polarization spectra at the peak time of the corresponding light curve at 300 keV for various bulk Lorentz factor Γ_0 . Top, middle and bottom panels show the spectra, PD spectra and PA spectra, respectively. The solid and dashed lines correspond to models of $[1b_i]$ and $[2b_i]$, respectively. The black, red, green, blue, and cyan lines correspond to $\Gamma_0 = 50, 100, 250, 500, \text{ and } 800$, respectively.

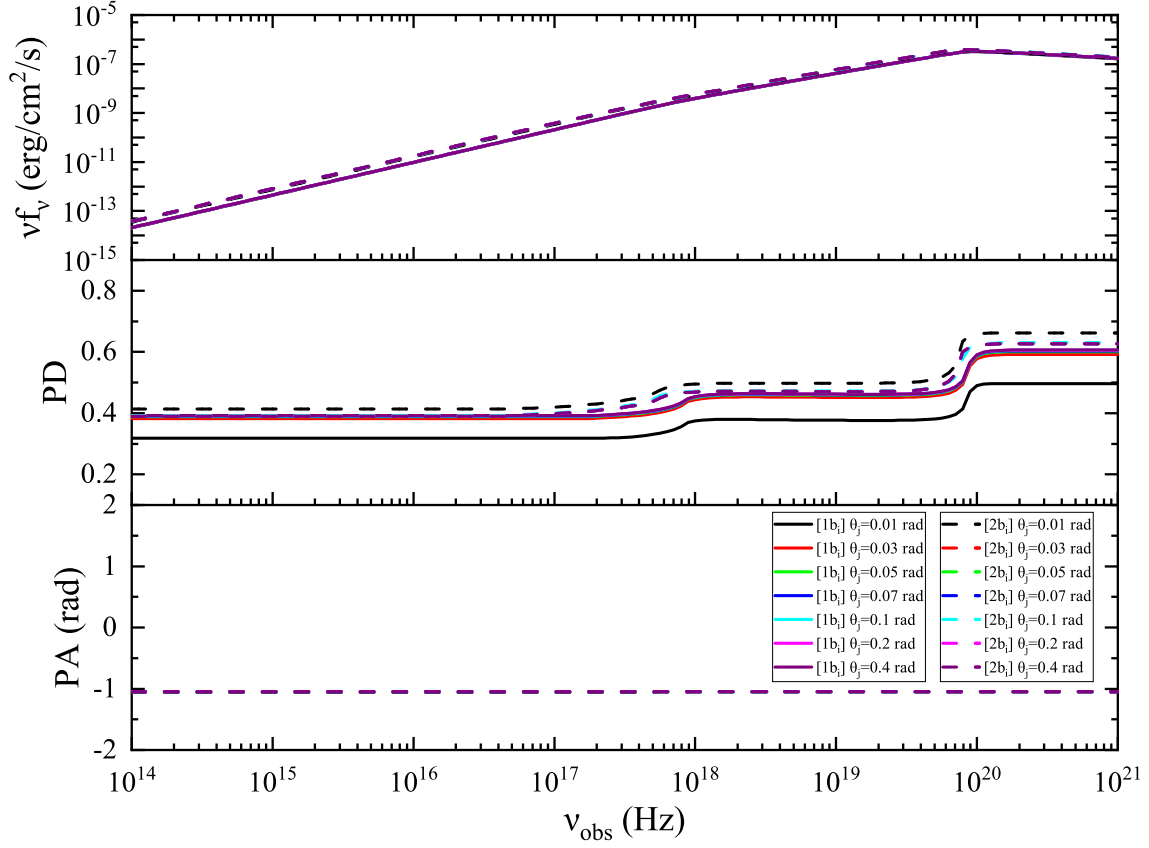


Figure B4. Spectra and polarization spectra at the peak time of the corresponding light curve at 300 keV for various jet opening angle θ_j . Top, middle and bottom panels show the spectra, PD spectra and PA spectra, respectively. The solid and dashed lines correspond to models of $[1b_i]$ and $[2b_i]$, respectively. The black, red, green, blue, cyan, magenta, and purple lines correspond to $\theta_j = 0.01, 0.03, 0.05, 0.07, 0.1, 0.2,$ and 0.4 rad, respectively.

REFERENCES

- Abbott, B. P., Abbott, R., Abbott, T. D., et al. 2017, *ApJL*, 848, L13
- Bégué, D., Siutsou, I. A., & Vereshchagin, G. V. 2013, *ApJ*, 767, 139
- Beloborodov, A. M. 2011, *ApJ*, 737, 68
- Beniamini, P., & Granot, J. 2016, *MNRAS*, 459, 3635
- Bloom, J. S., Kulkarni, S. R., Djorgovski, S. G., et al. 1999, *Nature*, 401, 453
- Cheng, K., Zhao, X., Mao, J., & Chen, Z. 2024, *A&A*, 687, A128
- Daigne, F., Bošnjak, Ž., & Dubus, G. 2009, in *American Institute of Physics Conference Series*, Vol. 1133, *Gamma-ray Burst: Sixth Huntsville Symposium*, ed. C. Meegan, C. Kouveliotou, & N. Gehrels (AIP), 288–293
- de Angelis, N., & Polar-2 Collaboration. 2022, in *37th International Cosmic Ray Conference*. 12-23 July 2021. Berlin, 580
- De Angelis, N., Burgess, J. M., Cadoux, F., et al. 2023, *arXiv e-prints*, arXiv:2309.00507
- Drenkhahn, G. 2002, *A&A*, 387, 714
- Eichler, D., & Levinson, A. 2000, *ApJ*, 529, 146
- Ghirlanda, G., Nappo, F., Ghisellini, G., et al. 2018, *A&A*, 609, A112
- Giannios, D. 2008, *A&A*, 480, 305
- Gill, R., & Granot, J. 2024, *MNRAS*, 527, 12178
- Gill, R., Granot, J., & Kumar, P. 2020, *MNRAS*, 491, 3343
- Gill, R., Kole, M., & Granot, J. 2021, *Galaxies*, 9, 82
- Goldstein, A., Veres, P., Burns, E., et al. 2017, *ApJL*, 848, L14
- Granot, J. 2016, *ApJL*, 816, L20
- Guan, & Lan. 2023, *Astronomy & Astrophysics*, 670, A160
- Hjorth, J., Sollerman, J., Møller, P., et al. 2003, *Nature*, 423, 847
- Lan, M.-X., & Dai, Z.-G. 2020, *ApJ*, 892, 141
- Lan, M.-X., Wang, H.-B., Xu, S., Liu, S., & Wu, X.-F. 2021, *ApJ*, 909, 184
- Lan, M.-X., Wu, X.-F., & Dai, Z.-G. 2016, *ApJ*, 816, 73
- . 2018, *ApJ*, 860, 44
- Lazzati, D., Morsony, B. J., & Begelman, M. C. 2009, *ApJL*, 700, L47
- Lazzati, D., Morsony, B. J., Margutti, R., & Begelman, M. C. 2013, *ApJ*, 765, 103
- Lazzati, D., Perna, R., Morsony, B. J., et al. 2018, *PhRvL*, 120, 241103
- Li, J.-S., Lan, M.-X., & Wang, H.-B. 2024, *ApJ*, 970, 10
- Lloyd-Ronning, N. M., Aykutalp, A., & Johnson, J. L. 2019, *MNRAS*, 488, 5823
- Lundman, C., Pe’er, A., & Ryde, F. 2013, *MNRAS*, 428, 2430
- Lundman, C., Vurm, I., & Beloborodov, A. M. 2018, *ApJ*, 856, 145
- MacFadyen, A. I., Woosley, S. E., & Heger, A. 2001, *ApJ*, 550, 410
- Mazzali, P. A., Deng, J., Tominaga, N., et al. 2003, *ApJL*, 599, L95
- Mészáros, P., & Rees, M. J. 2000, *ApJ*, 530, 292
- Mizuta, A., Nagataki, S., & Aoi, J. 2011, *ApJ*, 732, 26
- Nagakura, H., Ito, H., Kiuchi, K., & Yamada, S. 2011, *ApJ*, 731, 80
- Narayan, R., Paczynski, B., & Piran, T. 1992, *ApJL*, 395, L83
- Negro, M., Di Lalla, N., Omodei, N., et al. 2023, *ApJL*, 946, L21
- Oganesyan, G., Nava, L., Ghirlanda, G., & Celotti, A. 2017, *ApJ*, 846, 137
- . 2018, *A&A*, 616, A138
- Oganesyan, G., Nava, L., Ghirlanda, G., Melandri, A., & Celotti, A. 2019, *A&A*, 628, A59
- Paczynski, B., & Xu, G. 1994, *ApJ*, 427, 708
- Parsotan, T., & Lazzati, D. 2022, *ApJ*, 926, 104
- Parsotan, T., López-Cámara, D., & Lazzati, D. 2020, *ApJ*, 896, 139
- Pe’er, A., & Ryde, F. 2011, *ApJ*, 732, 49
- Poolakkil, S., Preece, R., Fletcher, C., et al. 2021, *ApJ*, 913, 60
- Ravasio, M. E., Ghirlanda, G., Nava, L., & Ghisellini, G. 2019, *A&A*, 625, A60
- Rees, M. J., & Meszaros, P. 1994, *ApJL*, 430, L93
- Rees, M. J., & Mészáros, P. 2005, *ApJ*, 628, 847
- Rouco Escorial, A., Fong, W., Berger, E., et al. 2023, *ApJ*, 959, 13
- Ruffini, R., Siutsou, I. A., & Vereshchagin, G. V. 2013, *ApJ*, 772, 11
- Rybicki, G. B., & Lightman, A. P. 1979, *Radiative processes in astrophysics*
- Sari, R. 1998, *ApJL*, 494, L49
- Sari, R., Piran, T., & Narayan, R. 1998, *ApJL*, 497, L17
- Sui, L.-Q., & Lan, M.-X. 2024, *MNRAS*, arXiv:2403.10718
- Thompson, C. 1994, *MNRAS*, 270, 480
- Toffano, M., Ghirlanda, G., Nava, L., et al. 2021, *A&A*, 652, A123
- Toma, K., Sakamoto, T., Zhang, B., et al. 2009, *The Astrophysical Journal*, 698, 1042
- Tomsick, J., Zoglauer, A., Sleator, C., et al. 2019, in *Bulletin of the American Astronomical Society*, Vol. 51, 98
- Uhm, Z. L., & Zhang, B. 2014, *Nature Physics*, 10, 351
- . 2015, *ApJ*, 808, 33

- . 2016, *ApJ*, 825, 97
- Uhm, Z. L., Zhang, B., & Racusin, J. 2018, *ApJ*, 869, 100
- Wang, H.-B., & Lan, M.-X. 2023a, *ApJ*, 946, 12
- . 2023b, arXiv e-prints, arXiv:2306.16618
- Woosley, S. E. 1993, *ApJ*, 405, 273
- Xu, M., Nagataki, S., Huang, Y. F., & Lee, S. H. 2012, *ApJ*, 746, 49
- Yu, H.-F., Preece, R. D., Greiner, J., et al. 2016, *A&A*, 588, A135
- Zhang, B., & Yan, H. 2011, *ApJ*, 726, 90